Cell Reports
Physical Science

Article

Capillarity cascade in crystalline micro-architectures for voxelated additive manufacturing

Graphical abstract

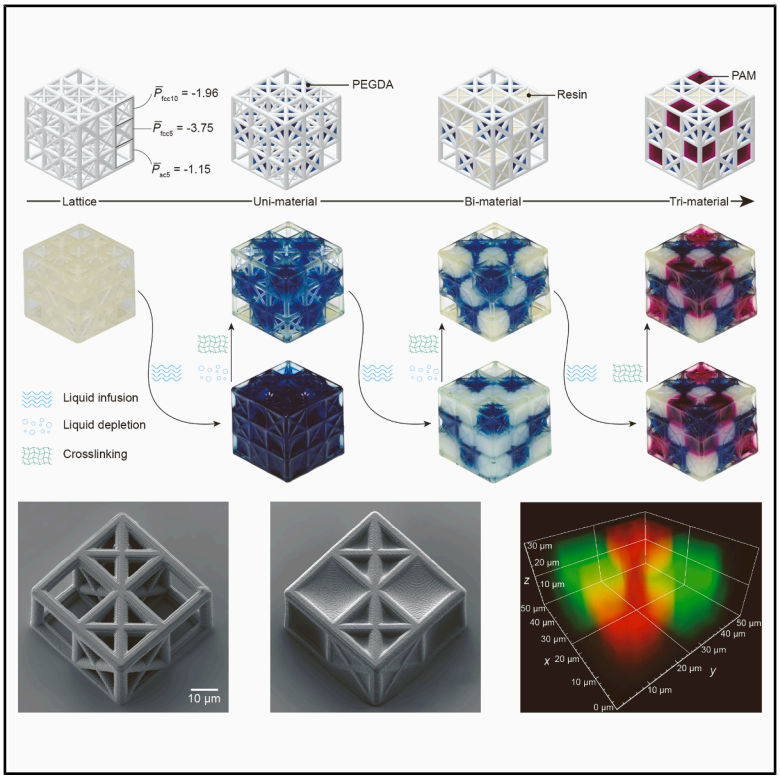

Authors

Hongtu Tan, Chunmei Zhou, Kai Zhuang, ..., Zuankai Wang, Xing Cheng, Xin Tang

Correspondence

chengx@sustech.edu.cn (X.C.), tangx@sustech.edu.cn (X.T.)

In brief

Tan et al. unfold a capillarity cascade phenomenon in crystalline micro-architectures, wherein lattice geometry dictates sequential liquid implosion. This mechanism enables high-resolution voxelated multi-material construction without tuning ink rheology.

Highlights

- Capillarity cascade occurs upon liquid dewetting in 3D micro-architectures
- Intercellular cascade sequence is ranked by imploding pressures of unit cells
- Capillarity cascade streamlines voxelated multi-material construction in high resolution

Tan et al., 2025, Cell Reports Physical Science 6, 102730
August 20, 2025
https://doi.org/10.1016/j.xcrp.2025.102730

CellPress

Cell Reports
Physical Science

CellPress
OPEN ACCESS

Article

Capillarity cascade in crystalline micro-architectures for voxelated additive manufacturing

Hongtu Tan,[1,2] Chunmei Zhou,[1,2] Kai Zhuang,[1,2] Caihong Liu,[1,2] Hongxuan Liang,[1,2] Zuankai Wang,[4] Xing Cheng,[3,*] and Xin Tang[1,2,5,*]

[1]Centre for Complex Flows and Soft Matter Research, Southern University of Science and Technology, Shenzhen, Guangdong, China
[2]Department of Mechanics and Aerospace Engineering, Southern University of Science and Technology, Shenzhen, Guangdong, China
[3]Department of Materials Science and Engineering, Southern University of Science and Technology, Shenzhen, Guangdong, China
[4]Department of Mechanical Engineering, The Hong Kong Polytechnic University, Hong Kong, China
[5]Lead contact
*Correspondence: chengx@sustech.edu.cn (X.C.), tangx@sustech.edu.cn (X.T.)
https://doi.org/10.1016/j.xcrp.2025.102730

SUMMARY

Stepwise cascade behavior marks numerous captivating phenomena. In a pre-filled crystalline micro-architecture, periodic polygon droplets, which adopt unit cells' shapes, dewet upon liquid depletion. Here, we show that, regardless of cells' spatial arrangement, those polygon droplets implode in a sequence ranked by lattice types, forming an intercellular dewetting order that is then termed the capillarity cascade. Such behavior is derived from unique imploding pressures associated with those lattices whose magnitudes originate from temporal adhesive and cohesive competition in the three-dimensional enclosed geometry. Using crystalline lattice engineering, liquid patterns can be well shaped through the capillarity cascade, which streamlines voxelated multi-material construction that features simplicity and high resolution. The capillarity cascade in a spatially periodic layout merits untold potential spanning an array of fields, including materials assembly, energy storage, and tissue modeling.

INTRODUCTION

Cascade behavior featuring a stepwise process without long-range leapfrogging underlines numerous phenomena that captivate long-lasting research interests, for example, energy cascade in turbulence,[1] reaction cascade in biochemicals,[2] and extinction cascade in biology.[3] Wetting in three-dimensional (3D) micro-architectures composed of periodic unit cells has been explored for liquid pumping or trapping through capillarity adhesion tuned by three-phase contact lines on micro-struts, leaving its reverse behavior, that is, dewetting in 3D micro-architectures, largely uncharted.[4,5]

Here, we observe liquid depletion in micro-architectures consisting of periodic struts linked in a way similar to that of crystallographic cubic Bravais lattices[6,7] and unfold a capillarity cascade behavior. In discrete cells, lattice frames anchor inward receding three-phase contact lines, modulating a Laplace pressure evolution through the competing adhesion and cohesion, which provides an imploding pressure unique to the cell's 3D geometry and surface wettability. When collectively connected, regardless of cell arrangements, the depletion drives sequential implosions ranked by lattice types, generating an intercellular capillarity cascade. Such sequential implosion is delineated by the imploding pressure, from high to low, in that order. The capillarity cascade is harnessed to pattern and deposit fluid in 3D space, which echoes and excels in voxelated multi-material construction with high simplicity and resolution and will be of interest and potential use to power source production,[8–11] catalysis distribution,[4,12–15] and mechanical metamaterial protection.[16–19]

RESULTS

Capillarity cascade in micro-architectures

As an analogy to crystallographic cubic Bravais lattices, we print an open architecture with micro-struts (edge length L = 2 mm, diameter D = 400 μm, and aspect ratio ϕ = 5) constructed in simple cubic (sc), body-centered cubic (bcc), and face-centered cubic (fcc) configurations using stereolithography (Figure 1A). After hydrophilic surface functionalization through oxygen plasma, water fully fills in the architecture with a volume of V_0 and is allowed to evaporate in the ambient condition (T_a = 24°C ± 1°C and relative humidity ≈40%). The polygon water shrinks in volume V with edges fixed by contact line pinning, creating competing dynamics wherein the cohesive force seeks to contract the droplet, which is deformed by the adhesive force. When the volume reaches a minimum permitted by geometry and wettability, the polygon droplet's neighboring surfaces coalesce, causing its implosion (Video S1). Such behavior is similar in discrete micro-architectures of different cell lattices, as shown in Figure 1B.

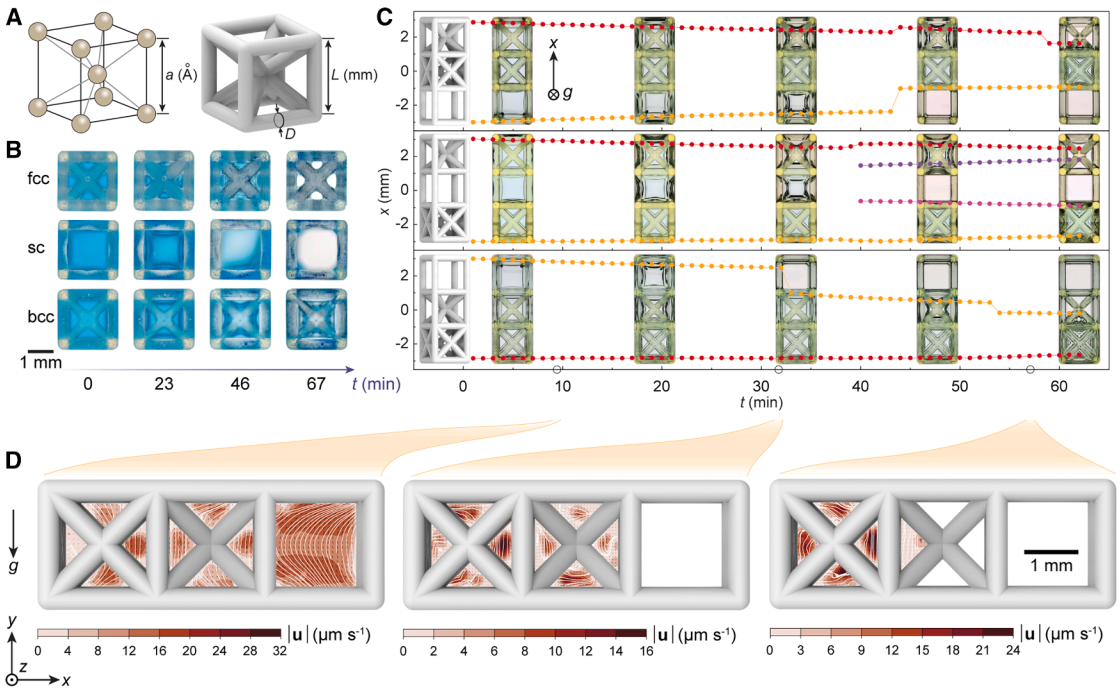

Figure 1. Stepwise capillarity cascade

(A) A bcc Bravais lattice (left) and the analogous bcc-architectured unit cell with an edge strut of L in length and D in diameter.

(B) Evaporation of water in discrete unit cells.

(C) Evaporation of water in tricellular architectures consisting of connected sc, fcc, and bcc in different arrangements. In the central axis of the tricellular structures, water surface translates and generates as a function of time. Regardless of arrangements, the imploding order appears monotonic in cellular types as water sequentially collapses in sc, bcc, and fcc cells. The open circles represent the moment when the velocity field in (D) is measured.

(D) PIV measurements are performed in the central plane of a tricellular architecture. Quasi-static evaporation sustains a weak natural convection with a characteristic velocity of ~10 μm s^{-1}, suggesting no strong pressure gradient among different cells. Water is dyed blue for visualization.

When those cells are collectively connected, implosions follow a specific sequence. As shown in Figure 1C and Video S2, regardless of the arrangement of tricellular architectures, polygon water consistently implodes in sc, bcc, and fcc cells in that order. Such imploding sequence and droplet collapsing volumes are highly consistent (Figure S1). We term such lattice-dependent sequential implosion the capillarity cascade.

To exclude a potential relationship between the capillarity cascade and liquid depletion flow, velocity fields demonstrated by particle image velocimetry (PIV) are shown in Figure 1D and Video S3. During the quasi-static evaporation (timescale ~10 min), the micro-architecture hosts gentle natural convection (u ~10 μm s^{-1}). Sustained by the buoyancy and temperature-driven Marangoni stress,[20–22] the creeping flow rises in the middle and sinks at two ends, forming two counter-rotating convective cells, a pattern similar to natural convection in an evaporating droplet. As the liquid volume decreases, the convective pattern remains unchanged and provides a negligible intercellular flux, suggesting a uniform pressure field in connected polygon droplets. Only upon transient implosion are liquid residues in the imploded cell driven by the surface tension γ and rapidly fed into the neighboring cell (u ~50 mm s^{-1}), providing a net intercellular flux (Figure S2; Video S4). Furthermore, as shown in Video S5, instead of quasi-static evaporation, we deplete infused liquid through negative-pressure extraction, and the capillarity cascade persists. However, it should be noted that the upper threshold of the liquid depletion rate is 4.6 μL s^{-1}, above which the capillarity cascade breaks (Figure S3). Below such a threshold, the capillarity cascade is caused by interfacial interaction rather than bulk flow, which we now investigate.

Implosion dynamics

We capture the pressure-volume relationship during liquid depletion in each cellular type through a phase-field method using the COMSOL Multiphysics (details in Note S1 and Figure S4). As shown in Figure 2A and Video S6, as the liquid volume shrinks, the locomotion of the contact line on the cellular structure (ϕ = 5 and water contact angle θ = 35°) is resisted, accompanied by a decrease in pressure. Polygon water droplets framed by struts feature unique collapsing volumes V_{min}, which are highlighted by the crosses in Figure 2A, below which they will implode. At the V_{min}, adjacent surfaces of the polygon droplet coalesce, perforating the water polygon and initiating the rapid implosion (insets in Figure 2A).

Accompanying the collapsing volume, the critical pressure, termed imploding pressure P_{min}, can be numerically derived through the surface curvature shaped by cohesive and adhesive competition in 3D geometry. By contrast, the conventional spherical approximation largely deviates from the numerical results. The capillarity surface is governed by the total-surface-energy

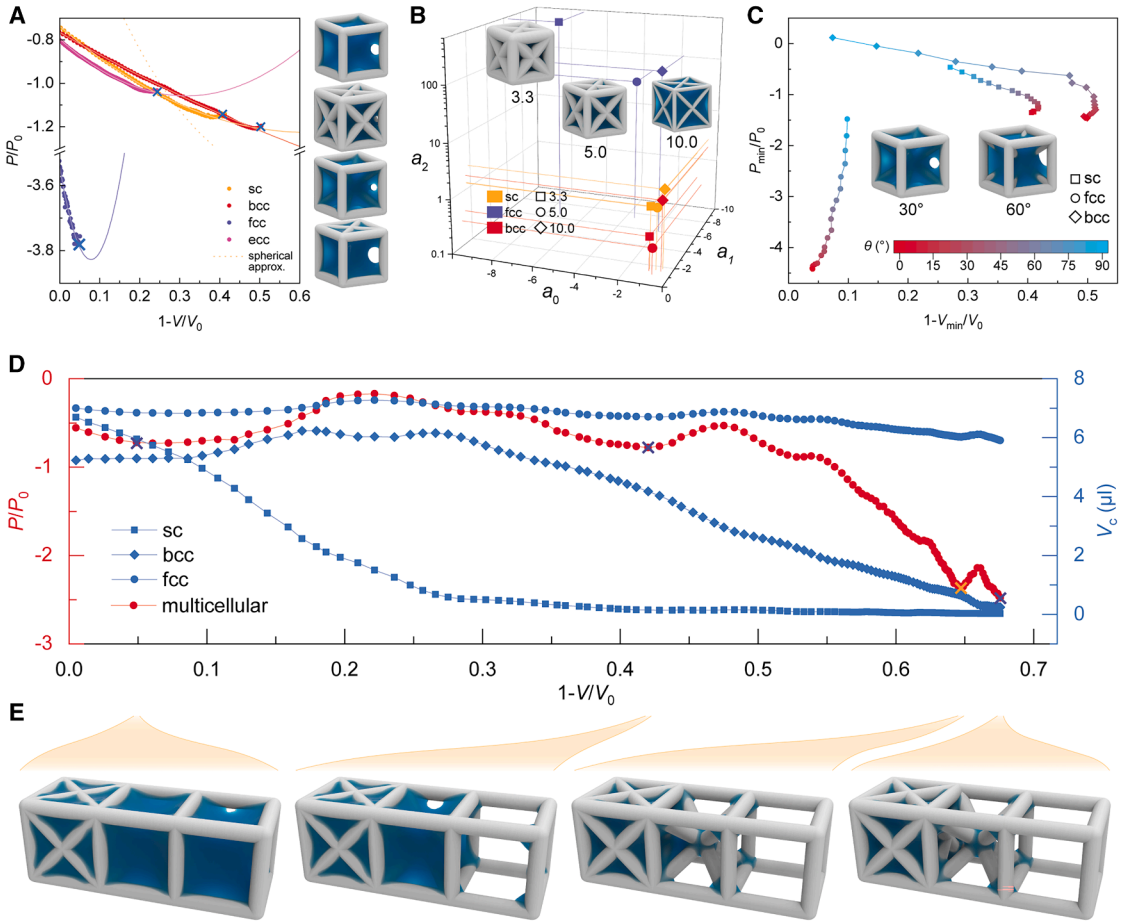

Figure 2. Cellular implosions

(A) Numerically calculated water pressure P normalized by that of equivalent droplet with the same initial volume, P_0, as a function of evaporated volume ratio $1\text{-}V/V_0$. Solid lines denote quadratic function fittings ($y = a_0 + a_1x + a_2x^2$), from which we deduce the fitting coefficients a_0, a_1, and a_2. The dashed line denotes the evolution of pressure in the sc cell, deduced using spherical approximation, wherein the water surface is considered a spherical cap truncated by the enclosing struts. Crosses denote instantaneous cellular implosions triggered by water film ruptures, from which we obtain the collapsing volumes V_{min} and implosion pressures P_{min}. Insets are numerically calculated water surfaces upon implosions.

(B) Quadratic function fitting coefficients as a function of the strut aspect ratio ϕ denoted by symbolic shape. Unlike the sc and bcc cells, the aspect ratio strongly impacts the coefficients of the fcc cell. Insets are fcc unit cells of different aspect ratios.

(C) Numerically calculated normalized implosion pressure P_{min}/P_0 and depleted collapsing volume ratio $1\text{-}V_{min}/V_0$ as a function of the strut wettability θ. Insets are numerically calculated water surfaces upon implosions for the bcc cells of contact angles of 30° and 60°, wherein water films rupture in different states.

(D) Numerically calculated normalized pressure P/P_0 and water volume in unit cells V_c as a function of depleted volume ratio for the tricellular architecture in (E). Purple and orange crosses denote, respectively, implosions of unit cells and the tetragonal pyramid inside the imploded bcc cell, which is shown in (E).

(E) Numerically calculated water surfaces of the tricellular architecture as a function of depleted volume ratio.

minimization, a fundamental principle generating two equations, that is, Young-Laplace equation $\Delta P = \gamma_{lv}\nabla\cdot\mathbf{n}$ for the liquid-vapor interface and Young's equation $\cos\theta = \frac{\gamma_{sv}-\gamma_{sl}}{\gamma_{lv}}$ for the three-phase contact line, where $\mathbf{n}$ is the outward unit normal vector and subscripts l, v, and s denote liquid, vapor, and solid, respectively.[23] The surface profile can be found by solving the Young-Laplace equation while constraining the boundaries to Young's equation. Unlike simple geometry, for example, a millimeter circular well wherein the liquid-vapor surface can be well described by the spherical-cap approximation, the micro-architecture complicates capillarity surface boundary in two aspects. At the strut's length scale, the polygon face enclosed by connected struts deforms the contact boundary, particularly at the corners, because of a capillary rise in the wedge (Figure S5). At the strut's radius scale, the strut's spherical cross-section introduces the position angle α, which locally changes the vertically apparent contact angle (Figure S6). The two factors enrich the controlling pathway for capillarity pressure evolution. Therefore, the complexity of the surface enclosed by struts cannot be sidestepped using the spherical cap approximation (Figures 2A and S7). P_{min} and V_{min} are reminiscent of yield strength and corresponding strain in tensile testing. Magnitudes of the P_{min} for different cellular types coincide with the implosion order in the tricellular architecture, that is, $P^{sc}_{min} > P^{bcc}_{min} > P^{fcc}_{min}$.

Evolution of the normalized pressure P/P_0, where P_0 is the pressure of spherical droplet with a volume equivalent to V_0 in sc, with respect to the depleted volume ratio $1 - V/V_0$ is nonlinear and can be fitted using a quadratic function ($y = a_0 + a_1x + a_2x^2$), from which we deduce the fitting coefficients a_0, a_1, and a_2 in Figure 2B. The impact of strut geometry on the pressure evolution profiles differs among cellular types. The variation in the strut aspect ratio (3.3–10.0) changes the fitting coefficients by a small amount for the sc and bcc cells but by a lot for the fcc cell.

The strut wettability modulates adhesive forces and thus the collapsing volume and subsequent imploding pressure. As shown in Figure 2C, as the strut becomes hydrophilic, the imploding pressure P_{min} monotonically decreases, whereas the collapsing volume V_{min} increases for the fcc cell but generally decreases and then slightly increases for the sc and bcc cells. The non-monotonic change of the V_{min} for the sc and bcc cells is due to strong liquid affinity on the edge struts (Figures 2C and S8). For a low contact angle ($\theta < 55°$), the liquid film of the polygon droplet ruptures at its center. Otherwise, the perforated hole appears at the corner (insets in Figure 2C).

The imploding pressure, regulated by the geometry and wettability of the micro-architecture, coaxes depleting liquid into the capillarity cascade. In a connected multicellular structure, the liquid's pressure is spatially uniform but decreases in magnitude during quasi-static depletion. Once the decreasing pressure reaches an imploding pressure, liquid in the corresponding cell collapses. In this way, polygon droplets collapse in order of imploding pressure from high to low. As shown in Figures 2D and 2E, we numerically study the evaporation in the tricellular architecture and trace the evolution of the normalized pressure P/P_0 and liquid volume V_c in each cell. Initially, the pressure decreases along with the decreasing volume until an imploding pressure for sc is reached. Then, the polygon droplet in the sc cell implodes, causing rapid lengthwise interfacial flow, which replenishes the other two cells. Such a pattern sequentially cycled for the bcc and, finally, fcc cells, generating a macroscopic capillarity cascade. Note that when the bcc droplet collapses, the remaining liquid is trapped inside the tetragonal pyramid, whose implosion ensues, a phenomenon consistent with the experiment. The numerical study portrays the interfacial behavior, unfolding the role played by the implosion dynamics in the capillarity cascade.

Voxelated multi-materials

The salient feature of the capillarity cascade, that is, temporal liquid deposition in 3D space, echoes the requirements of voxelated multi-material printing. The programming function and composition of the materials at the voxel level promise huge application potential.[24,25] Nevertheless, its ready materialization is still challenged by the tuning of multi-inks' rheology, the design of the microfluidic printhead, and coordination between the feeding and moving mechanical modules.[26] The capillarity cascade provides a simplified alternative to constructing voxelated multi-materials.

As the fcc lattice's imploding dynamics can be regulated by the strut aspect ratio across a wide range, it becomes a preferred configuration for our voxelated multi-material framework (Figure 2B). As shown in Figures 3A and 3B, a micro-architecture consisting of three lattices, fcc5, fcc10, and sc5, where the number denotes the strut aspect ratio, is fabricated. Then, the polyethylene glycol diacrylate (PEGDA) precursor solution is infused with liquid, and depletion ensued. Consistent with the capillarity cascade, droplets in cells of higher imploding pressure (fcc10 and sc5) collapse, leaving the liquid only housed by the cell of the lowest imploding pressure (fcc5), whereupon the depletion is stopped (Video S5). The volumetrically deposited precursor is then crosslinked into hydrogel cubes. By cycling the infusion-depletion-crosslinking step, photoresin and polyacrylamide (PAM) gel, respectively, are sequentially deposited in fcc10 and sc5, producing a tri-material matrix. Unlike conventional printing, where multi-material building blocks are built up voxel by voxel, our method assembles a collection of the same volumetric elements in a single step, which is in a phase-by-phase manner, improving time efficiency. In Figure 3C, after the initial lattice scaffold is printed, we fabricate a $9 \times 9 \times 3$ tri-material matrix in only three steps.

The volumetric elements are seamlessly bonded. To examine this, we fabricate an electric-eel-inspired power source through the capillarity cascade. The electric unit consists of high-salt, cation-selective, low-salt, anion-selective, and another high-salt compartments, making it a quad-material matrix[8,9] (Note S2). As shown in Figures 3E and 3F, after fabrication, the open-circuit voltage V_{oc}, which scales with units in series, and the short-circuit current I_{sc}, which scales with units in parallel, can be measured. The seamless interfacial bonding bridges the ionically conductive pathway, which produces diffusion potential under an ionic gradient.

The construction of a voxelated matrix in the resin scaffold through the capillarity cascade requires only that the material precursor is in the liquid phase, a feature that broadens the range of materials that can be manufactured irrespective of their rheological properties. Moreover, such a practical alternative appears as a paradigm shift in stereolithography, as multi-materials are effortlessly patterned after the initial resin scaffold is printed.

Microscale resolution

The resolution of extrusion-based 3D voxelated printing is dictated by the printing nozzle, whose size is a compromise between driving pressure and ink rheology. As a result, the printed voxel is frequently limited to a length scale of ~1 mm. As the capillarity cascade integrates voxelated 3D printing into the thriving stereolithography system without needing to remodify their configuration or ink, we explore the resolution limit of our method by printing the lattice scaffold through two-photon polymerization.

The printed $2 \times 2 \times 1$ lattice consists of fcc5 and sc5 cells of a side length of 20 μm (Figures 4A and 4B). As shown in Figure 4A and Video S7, by following the abovementioned construction procedure, a 25 vol % photoresin-in-ethanol solution is firstly infused into the lattice. Upon complete depletion of the ethanol solvent through evaporation, fcc cells are filled with the HTL (high-temperature liquid) photoresin and are subsequently UV crosslinked. Then, a similar procedure is repeated to fill and crosslink TRU (tough resin ultra) photoresin in sc cells. In this way, a voxelated multi-material of a voxel side length of 20 μm

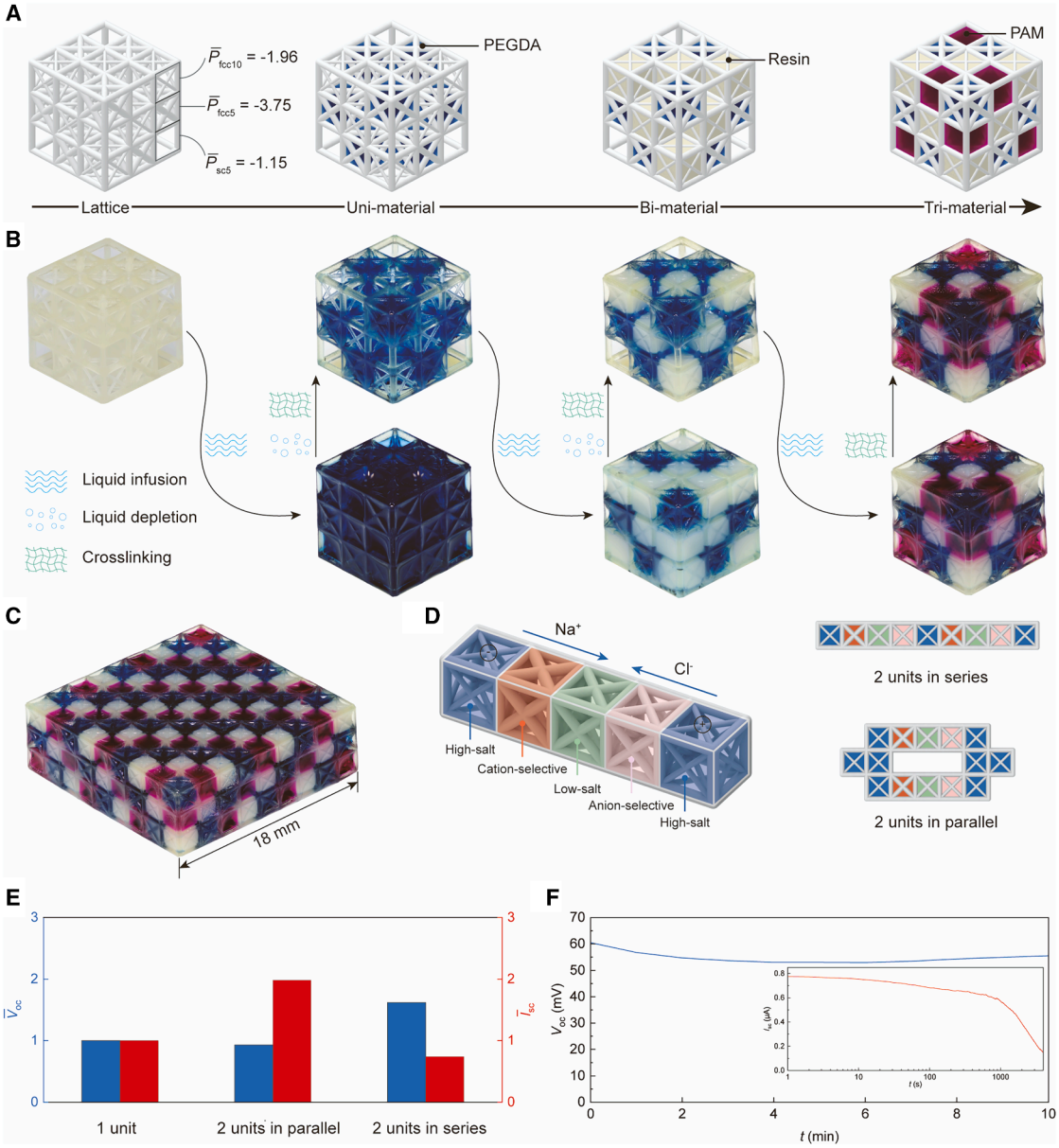

Figure 3. Voxelated multi-materials

(A) Voxelated multi-material printing through capillarity cascade in a micro-architecture consisting of fcc5, fcc10, and sc5.

(B) The hydrogel precursor or photoresin solution is infused into the micro-architecture and then depleted by evaporation or extraction. Liquid in cells collapses in order of imploding pressure and is distributed into cells of the lowest imploding pressure before drying out. Those liquid residues are crosslinked or cured, forming selectively patterned voxels. Such steps are cycled for multi-material construction.

(C) A 9 × 9 × 3 voxelated multi-material consisting of PEGDA, resin, and PAM cubes is fabricated in three steps.

(D) Electric-eel-inspired power sources consisting of four different materials in series and parallel configurations are fabricated through capillarity cascade in a framework consisting of fcc10, fcc6, fcc4.29, and fcc3.33.

(E) Open-circuit voltage and short-circuit current of the hydrogel power sources in different configurations normalized by that of a gel cell unit.

(F) Temporal evolution of open-circuit voltage and short-circuit current for a gel cell unit.

is successfully constructed, improving the resolution of voxelated 3D printing by 100-fold (Figure 4C).

The inter-voxel interface is examined using laser scanning confocal microscopy by respectively dying the HTL photoresin with perylene red and the TRU photoresin with Rhodamine 6G. As shown in Figure 4D, the interface appears sharp, implying the absence of material mixing. The capillarity cascade effects even at micrometer scale, a feature that allows it to fully explore the possibility of the most advanced stereolithography, and their integration

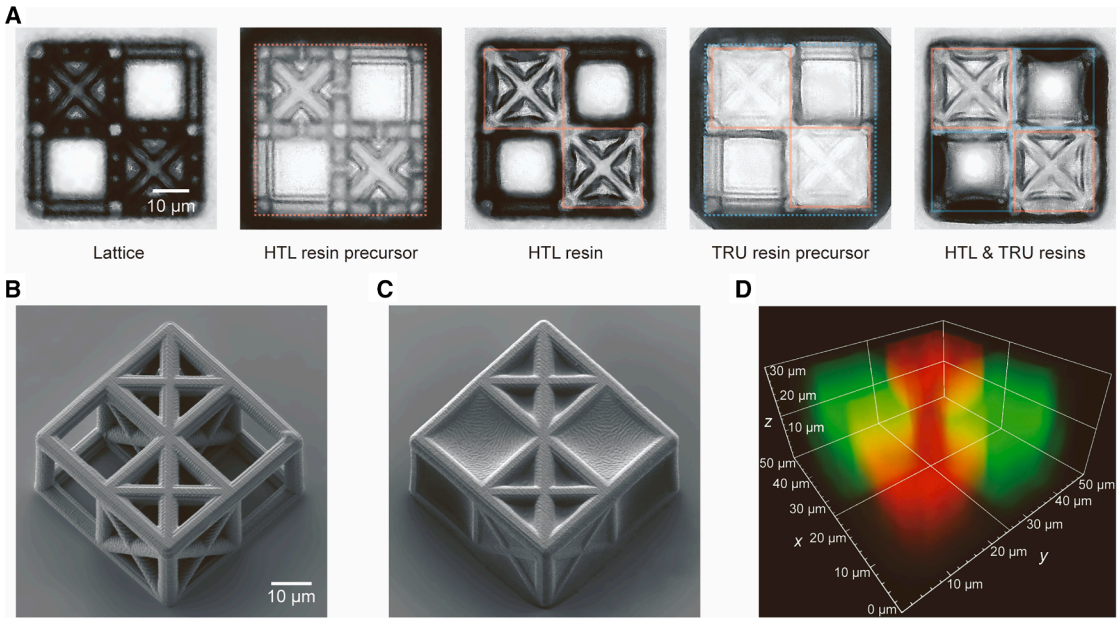

Figure 4. Microscale voxelated multi-materials

(A) Microscale voxelated multi-material fabricated through capillarity cascade. A 25 vol % HTL photoresin-in-ethanol solution is infused into the microscale lattice scaffold, followed by heating to fully evaporate the ethanol, leaving resin in fcc cells that is then crosslinked through UV light. Similarly, TRU photoresin is distributed in sc cells and then crosslinked. Dashed and solid lines denote precursor liquid and crosslinked resin, respectively. Red and blue colors denote HTL and TRU resins, respectively.

(B and C) Scanning electron microscopy images show the microscale lattice scaffold printed using two-photon polymerization (B) and the corresponding voxelated bi-material fabricated through capillarity cascade (C).

(D) Laser scanning confocal microscopy image shows the sharp interface between two resins. For visualization, HTL and TRU photoresins are dyed with perylene red (red) and Rhodamine 6G (green), respectively.

unlocks high resolution and simplicity for nascent voxelated 3D printing.

DISCUSSION

We present a capillarity cascade in crystalline micro-architectures upon liquid depletion. The capillarity cascade is derived from contrastive imploding pressures for different cellular types, a result caused by competitive cohesive and adhesive interactions in 3D configurations. Regardless of depletion manner and cell arrangements, polygon water droplets sequentially implode in sc, bcc, and fcc cells, in that order, generating anisotropic dewetting behavior. Through crystalline lattice engineering, we harness 3D liquid deposition and patterning, providing a simplified, highly precise, and time-efficient alternative to voxelated multi-material printing. Clearly, such cascade behavior works at the capillary length for various complex structures formed by different unit cells, spanning a long imploding sequence and a wide variety of liquid properties (Figures S9–S11). Even in a different scenario, for example, upon fog deposition, the growth of the contained liquid exhibits a reverse capillarity cascade, implying the generality of the phenomenon (Figure S12; Video S8).

This work uncovers a dewetting behavior upon liquid depletion in complex geometry and provides a way to pattern and organize liquids in 3D space with controllability, programmability, and performance. The consecutive transport behavior may unfold the corroding positions, thus enabling the design of protection pathways for metamaterials in aerospace and ocean engineering where condensates or aerosols will be deposited and translated among the micro-/nano-structures whose periodic arrangement enables exceptional combinations of mechanical properties.[6,7,17] It is also relevant to the electrolyte delivery in electrodes, which are frequently textured with macro-/meso-porous structures for a higher gravimetric capacity and power density in lithium-ion batteries and supercapacitors.[27,28] The flow control in 3D space may allow the localization of cells, biomolecule solutions, and micronutrients, a feature important in recapitulating volumetric microenvironments for 3D tissue modeling and engineering.[5,22,29,30] In general, the findings of this work merit technological potential for many fields, such as energy storage,[31] 3D material constructions,[5] and anti-corrosion of mechanical metamaterials.[16]

METHODS

Crystalline micro-architectures are fabricated out of photosensitive resins (Boston Micro Fabrication, HTL resin or TRU resin, Anycubic) using projection microstereolithography printers (Boston Micro Fabrication S240 or Anycubic M3 Max) with 10 μm optical resolution. For the hydrophilic surface functionalization, the printed micro-architectures are treated with oxygen

plasma (SETCAS SC-PE-I) for 5 min, followed by a 10 min aging, ensuring that the surface wettability remains stable for subsequent experiments (Figure S13). Water is dyed with methylene blue for visualization and infused into the architectures using a syringe. The ambient temperature is controlled at 24°C ± 1°C, and the relative humidity is set at approximately 40%.

Quasi-static evaporation is recorded using a stereomicroscope (Olympus SZ61TR) coupled with a charge-coupled device (CCD) camera. The rapid interfacial flow and PIV are recorded using high-speed photography at up to 4,000 frames per second (Photron UX50). For PIV analysis, polystyrene microspheres of 20 μm in diameter are doped as tracer particles, producing typical Stokes numbers ($St = \rho_{ps} D_{ps} u / 18\mu$) of 0.1 for implosion and 0.0001 for convection. The velocity field is analyzed using an open-source MATLAB code, PIVlab.

To construct voxelated multi-materials, liquid can be depleted through either evaporation or extraction. The precursor in different concentrations is used for different depletion methods. Using evaporation, a mixture of 33 vol % PEGDA aqueous solution and 2 wt % 2-hydroxy-2-methylpropiophenone (the photoinitiator) is used as the precursor for PEGDA gel, and 50 vol % photoresin-in-ethanol solution is used as the precursor for resin (standard resin, Anycubic). Using extraction, the concentration of PEGDA aqueous solution is changed to 50 vol %, and the photoresin is used without ethanol dilution. Because PAM is the last material that is filled in without depletion, its precursor is prepared as a mixture of 5.5 M acrylamide, 0.066 M N,N′-methylenebisacrylamide (bis), and 0.615 M photoinitiator. Hydrogels and photoresin precursors are spatially patterned through the capillarity cascade and then crosslinked using UV light. At the liquid-filling step, the previously crosslinked solid cubes occupy the space; thus, the liquid naturally fills the empty cells.

To fabricate the soft power source, precursors of four gels are prepared. The high-salt hydrogel precursor is a mixture of 0.5 M NaCl, 5.4 M acrylamide, 0.067 M bis, and 0.0615 M photoinitiator. The low-salt hydrogel precursor is a mixture of 0.015 M NaCl, 5.5 M acrylamide, 0.066 M bis, and 0.615 M photoinitiator. The cation-selective hydrogel precursor is a mixture of 2 M 2-acrylamido-2-methylpropane sulfonic acid, 3.7 M acrylamide, 0.045 M bis, and 0.0615 M photoinitiator. The anion-selective hydrogel precursor is a mixture of 2 M (3-acrylamidopropyl) trimethylammonium chloride, 2.75 M acrylamide, 0.034 M bis, and 0.0615 M photoinitiator. Hydrogel precursors are selectively arranged through the capillarity cascade and sequentially crosslinked using UV light.

Microscale micro-architectures are fabricated using two-photon polymerization (Nanoscribe, Photonic Professional GT2) on a glass substrate at a controlled temperature of 25°C. Then, the glass along with the printed structure undergoes a liquid-like surface modification to avoid excess liquid retention. The modification solution is made by mixing isopropanol, dimethyldimethoxysilane, and sulfuric acid at a mass ratio of 100:10:1. The glass is treated with oxygen plasma and then dip coated in the prepared solution for 5 s. Excess liquid is removed using an absorbent paper. The samples are naturally dried at room temperature and then subsequently rinsed with water, isopropanol, and cyclohexane. To infuse the lattice with firstly HTL and then TRU resin precursors, we simply tilt the glass and let a droplet of precursor solution flow across the lattices. The fabricated microscale voxelated multi-material is then examined using laser scanning confocal microscopy (Olympus FV3000) and scanning electron microscopy.

For fog deposition, fine mist generated by a humidifier (AUX AJ-H860) flows toward the micro-architecture at a rate of 1.2 L h^{-1}.

RESOURCE AVAILABILITY

Lead contact

Requests for further information, resources, or materials should be directed to and will be fulfilled by lead contact, Professor Xin Tang (tangx@sustech.edu.cn).

Materials availability

This study did not generate new unique materials.

Data and code availability

- All data are available in the main text or the supplemental information.
- This paper did not generate original code.
- Any additional information required to reanalyze the data reported in this paper is available from the lead contact upon request.

ACKNOWLEDGMENTS

We thank Prof. Shidi Huang, Prof. Huanshu Tan, and Prof. Yahui Xue for equipment support and Dr. Haibo Zhao and Dr. Yang Qi for discussion. X.T. acknowledges funding from the National Natural Science Foundation of China (12302354), the Shenzhen Medical Research Fund (A2303048), the Shenzhen Science and Technology Program (JCYJ20220530114417040), and the Southern University of Science and Technology (Y01646103).

AUTHOR CONTRIBUTIONS

X.T. and H.T. conceived and designed the project. H.T. performed the experiments and numerical studies. X.T., H.T., X.C., and Z.W. analyzed the data. X.T. and H.T. wrote the manuscript with comments from all other authors.

DECLARATION OF INTERESTS

The authors declare no competing interests.

SUPPLEMENTAL INFORMATION

Supplemental information can be found online at https://doi.org/10.1016/j.xcrp.2025.102730.

Received: April 10, 2025
Revised: June 10, 2025
Accepted: July 4, 2025
Published: July 30, 2025

REFERENCES

1. Wang, J., Wan, M., Chen, S., Xie, C., Wang, L.P., and Chen, S. (2019). Cascades of temperature and entropy fluctuations in compressible turbulence. J. Fluid Mech. *867*, 195–215.
2. Wang, H., Zhao, Z., Liu, Y., Shao, C., Bian, F., and Zhao, Y. (2018). Biomimetic enzyme cascade reaction system in microfluidic electrospray microcapsules. Sci. Adv. *4*, eaat2816.
3. Sanders, D., Thébault, E., Kehoe, R., and Frank van Veen, F. (2018). Trophic redundancy reduces vulnerability to extinction cascades. Proc. Natl. Acad. Sci. *115*, 2419–2424.
4. Dudukovic, N.A., Fong, E.J., Gemeda, H.B., DeOtte, J.R., Cerón, M.R., Moran, B.D., Davis, J.T., Baker, S.E., and Duoss, E.B. (2021). Cellular fluidics. Nature *595*, 58–65.

5. Yasuga, H., Iseri, E., Wei, X., Kaya, K., Di Dio, G., Osaki, T., Kamiya, K., Nikolakopoulou, P., Buchmann, S., Sundin, J., et al. (2021). Fluid interfacial energy drives the emergence of three-dimensional periodic structures in micropillar scaffolds. Nat. Phys. *17*, 794–800.
6. Schaedler, T.A., and Carter, W.B. (2016). Architected cellular materials. Annu. Rev. Mater. Res. *46*, 187–210.
7. Pham, M.-S., Liu, C., Todd, I., and Lertthanasarn, J. (2019). Damage-tolerant architected materials inspired by crystal microstructure. Nature *565*, 305–311.
8. Schroeder, T.B.H., Guha, A., Lamoureux, A., VanRenterghem, G., Sept, D., Shtein, M., Yang, J., and Mayer, M. (2017). An electric-eel-inspired soft power source from stacked hydrogels. Nature *552*, 214–218.
9. Zhang, Y., Riexinger, J., Yang, X., Mikhailova, E., Jin, Y., Zhou, L., and Bayley, H. (2023). A microscale soft ionic power source modulates neuronal network activity. Nature *620*, 1001–1006.
10. Jiang, M., Wang, Y., Liu, F., Du, H., Li, Y., Zhang, H., To, S., Wang, S., Pan, C., Yu, J., et al. (2022). Inhibiting the Leidenfrost effect above 1,000 C for sustained thermal cooling. Nature *601*, 568–572.
11. Tang, X. (2022). Multifunctional droplet-surface interaction effected by bulk properties. Droplet *2*, e38.
12. Liu, L., and Corma, A. (2020). Confining isolated atoms and clusters in crystalline porous materials for catalysis. Nat. Rev. Mater. *6*, 244–263.
13. Lee, B., Kim, S., Ko, J., Lee, S.R., Kim, Y., Park, S., Kim, J., Hyung, S., Kim, H.Y., and Jeon, N.L. (2022). 3D micromesh-based hybrid bioprinting: multidimensional liquid patterning for 3D microtissue engineering. NPG Asia Mater. *14*, 6.
14. Zhang, Y., Huang, Z., Qin, F., Wang, H., Cui, K., Guo, K., Cai, Z., Cai, X., Xiao, J., Carmeliet, J., et al. (2024). Connected three-dimensional polyhedral frames for programmable liquid processing. Nat. Chem. Eng. *1*, 472–482.
15. Cao, J., and Tao, S. (2024). Liquid-liquid reactions performed by cellular reactors. Nat. Commun. *15*, 5579.
16. Wang, Y., Li, L., Hofmann, D., Andrade, J.E., and Daraio, C. (2021). Structured fabrics with tunable mechanical properties. Nature *596*, 238–243.
17. Zheng, X., Smith, W., Jackson, J., Moran, B., Cui, H., Chen, D., Ye, J., Fang, N., Rodriguez, N., Weisgraber, T., and Spadaccini, C.M. (2016). Multiscale metallic metamaterials. Nat. Mater. *15*, 1100–1106.
18. Feng, S., Zhu, P., Zheng, H., Zhan, H., Chen, C., Li, J., Wang, L., Yao, X., Liu, Y., and Wang, Z. (2021). Three-dimensional capillary ratchet-induced liquid directional steering. Science *373*, 1344–1348.
19. Hong, Y., Liu, S., Yang, X., Hong, W., Shan, Y., Wang, B., Zhang, Z., Yan, X., Lin, W., Li, X., et al. (2024). A bioinspired surface tension-driven route toward programmed cellular ceramics. Nat. Commun. *15*, 5030.
20. Hegseth, J.J., Rashidnia, N., and Chai, A. (1996). Natural convection in droplet evaporation. Physical review E *54*, 1640–1644.
21. Bartashevich, M.V., Marchuk, I.V., and Kabov, O.A. (2012). Numerical simulation of natural convection in a sessile liquid droplet. Thermophys. Aeromech. *19*, 317–328.
22. Chen, Z., Peng, K., and Xu, B. (2023). Material assembly by droplet drying: From mechanics theories to applications. Droplet *2*, e76.
23. Ruiz-Gutiérrez, É., Guan, J.H., Xu, B., McHale, G., Wells, G.G., and Ledesma-Aguilar, R. (2017). Energy Invariance in Capillary Systems. Phys. Rev. Lett. *118*, 218003.
24. Skylar-Scott, M.A., Mueller, J., Visser, C.W., and Lewis, J.A. (2019). Voxelated soft matter via multimaterial multinozzle 3D printing. Nature *575*, 330–335.
25. Cheng, J., Wang, R., Sun, Z., Liu, Q., He, X., Li, H., Ye, H., Yang, X., Wei, X., Li, Z., et al. (2022). Centrifugal multimaterial 3D printing of multifunctional heterogeneous objects. Nat. Commun. *13*, 7931.
26. He, P., Yue, J., Qiu, Z., Meng, Z., He, J., and Li, D. (2024). Consecutive multimaterial printing of biomimetic ionic hydrogel power sources with high flexibility and stretchability. Nat. Commun. *15*, 5261.
27. Bai, P., and Bazant, M.Z. (2014). Charge transfer kinetics at the solid–solid interface in porous electrodes. Nat. Commun. *5*, 3585.
28. Liu, Z., Yuan, X., Zhang, S., Wang, J., Huang, Q., Yu, N., Zhu, Y., Fu, L., Wang, F., Chen, Y., and Wu, Y. (2019). Three-dimensional ordered porous electrode materials for electrochemical energy storage. NPG Asia Mater. *11*, 12.
29. Choe, M.M., Tomei, A.A., and Swartz, M.A. (2006). Physiological 3D tissue model of the airway wall and mucosa. Nat. Protoc. *1*, 357–362.
30. Cui, H., Tronser, T., Wang, X., Wesslowski, J., Davidson, G., Popova, A.A., and Levkin, P.A. (2022). High-throughput formation of miniaturized cocultures of 2D cell monolayers and 3D cell spheroids using droplet microarray. Droplet *2*, e39.
31. He, J., Lu, C., Jiang, H., Han, F., Shi, X., Wu, J., Wang, L., Chen, T., Wang, J., Zhang, Y., et al. (2021). Scalable production of high-performing woven lithium-ion fibre batteries. Nature *597*, 57–63.